

Growth, characterization and Chern insulator state in MnBi_2Te_4 via the chemical vapor transport method

Chaowei Hu,¹ Anyuan Gao,² Bryan Stephen Berggren,³ Hong Li,⁴ Rafał Kurlito,³
Dushyant Narayan,³ Ilija Zeljkovic,⁴ Dan Dessau,³ Suyang Xu,² and Ni Ni^{1,*}

¹*Department of Physics and Astronomy and California NanoSystems Institute,
University of California, Los Angeles, CA 90095, USA*

²*Department of Chemistry and Chemical Biology, Harvard University, Cambridge, MA, USA*

³*Department of Physics and Center for Experiments on Quantum Materials,
University of Colorado, Boulder, CO 80309, USA*

⁴*Department of Physics, Boston College, Chestnut Hill, MA 02467, USA*

(Dated: October 13, 2021)

As the first intrinsic antiferromagnetic topological insulator, MnBi_2Te_4 has provided a platform to investigate the interplay of band topology and magnetism as well as the emergent phenomena arising from such an interplay. Here we report the chemical-vapor-transport (CVT) growth and characterization of MnBi_2Te_4 , as well as the observation of the field-induced quantized Hall conductance in 6-layer devices. Through comparative studies between our CVT-grown and flux-grown MnBi_2Te_4 via magnetic, transport, scanning tunneling microscopy, and angle-resolved photoemission spectroscopy measurements, we find that CVT-grown MnBi_2Te_4 is marked with higher Mn occupancy on the Mn site, slightly higher Mn_{Bi} antisites, smaller carrier concentration and a Fermi level closer to the Dirac point. Furthermore, a 6-layer device made from the CVT-grown sample shows by far the highest mobility of $2500 \text{ cm}^2\text{V}^{-1}\text{s}^{-1}$ in MnBi_2Te_4 devices with the quantized Hall conductance appearing at 1.8 K and 8 T. Our study provides a new route to obtain high-quality single crystals of MnBi_2Te_4 that are promising to make superior devices and realize emergent phenomena, such as the layer Hall effect and quantized anomalous hall effect, etc.

I. INTRODUCTION

Magnetic topological insulators (MTI) are a rising family of quantum materials that host both nontrivial band topology and magnetic order, providing a fruitful platform to realize emergent quantum phenomena such as the quantum anomalous Hall effect (QAHE), axion insulator state, quantum magnetoelectric effect, etc.¹⁻³ Recently, MnBi_2Te_4 was proposed to be the first intrinsic candidate of MTI⁴⁻²¹. It is composed of Te-Bi-Te-Mn-Te-Bi-Te septuple layers (SL) which are weakly bonded by van der Waals force as shown in Fig. 1(a). The van der Waals nature makes it possible to exfoliate a bulk MnBi_2Te_4 crystal into nm-thick thin flakes where QAHE was observed at a record high temperature in 5-layer devices^{15,16}. Previously, MnBi_2Te_4 single crystals were grown via the flux method with Bi_2Te_3 ¹² or MnCl_2 ¹⁵ as the flux or from the melt of the stoichiometric mixture⁸. Other members of the $\text{MnBi}_{2n}\text{Te}_{3n+1}$ (MBT) family ($n > 1$) can also be synthesized using the Bi_2Te_3 flux^{5,9,21-36}.

Chemical defects are observed in the MBT family. For flux-grown MnBi_2Te_4 , studies find that 18(1) % of Mn sites are occupied by Bi atoms²¹ while only 1-4% of Bi sites are occupied by Mn atoms^{13,21,37-39}. Mn and Bi sites, as well as the antisite defects are displayed in Fig. 1 (a). This chemical complexity leads to electron carrier concentration on the order of 10^{20} cm^{-3} in samples grown by flux method or from stoichiometric melting^{11,12,40}. Besides making the sample heavily- n doped, chemical defects have profound impacts on the magnetism and band topology of MBT compounds. Antisites result in additional Mn sublattices in MBT. While

the effect is relatively weak in MnBi_2Te_4 , it is exaggerated in MnSb_2Te_4 ⁴¹, Sb-doped MnBi_2Te_4 ³⁹ and Sb-doped MnBi_4Te_7 ⁴² since sizable amount of Mn_{Sb} antisites are introduced when Sb atoms are present in the lattice, leading to ferrimagnetic ground states. From the aspect of band topology, large amount of Mn_{Sb} antisites can be detrimental to non-trivial band topology in MBT^{41,42}. Because the QAHE is proposed theoretically on the ideal MnBi_2Te_4 structure, the defects which have caused the aforementioned complications may hinder the exploration of QAHE in MBT. Therefore, growth of single crystals that have a lower carrier concentration, fewer defects and higher magnetic homogeneity is highly desired for the exploration of various emergent phenomena and future applications of the material.

In this work, we report a new single crystal growth route of MnBi_2Te_4 via chemical vapor transport (CVT) using I_2 as transport agent. We find that a small thermal gradient is sufficient to drive the CVT growth and allows a good control of growth. Through magnetic, transport and spectroscopic measurements, we show the carrier density is greatly reduced in the CVT-grown samples. Chern insulator state is observed in a 6-SL device with the highest reported mobility. All evidence points to a new promising growth route so that enhanced functionality of the devices can be made.

II. EXPERIMENTAL METHODS

Single crystals of MnBi_2Te_4 were grown using CVT method with I_2 as the transport agent. X-ray diffrac-

tion was collected using a PANalytical Empyrean diffractometer (Cu K- α radiation) on the (00 L) surface to confirm the MnBi₂Te₄ phase. Wavelength-dispersive spectroscopy (WDS) was conducted on the bulk sample to determine the elemental ratio of single crystals. To address the sensitive chemical nature of 2D MnBi₂Te₄ flakes, all fabrication processes were completed in an argon environment without exposure to air, chemicals, or heat in a glovebox/evaporator assembly. Thin flakes of MnBi₂Te₄ were mechanically exfoliated from the bulk crystal onto the SiO₂/Si wafers using Scotch-tape. We then evaporated gold contacts by a pre-made stencil mask. Finally, BN and graphite flakes were transferred onto the MnBi₂Te₄ flake as the top gate.

Magnetization data were measured in a Quantum Design (QD) Magnetic Properties Measurement System (QD MPMS). Electric resistivity for both bulk samples and devices were measured in a QD DynaCool Physical Properties Measurement System (DynaCool PPMS). Longitudinal and Hall voltages were measured simultaneously using standard lock-in techniques. The gate voltages were applied by Keithley 2400 source meters.

Scanning tunneling microscopy (STM) data was acquired using a customized Unisoku USM1300 microscope. Single crystals were cleaved at room temperature in ultra-high vacuum (UHV) pressure of about 1×10^{-10} Torr and immediately inserted into the STM chamber where they were kept at 4.5 K during the measurements. Spectroscopic measurements were made using a standard lock-in technique with 915 Hz frequency and bias excitation as detailed in figure captions. STM tips used were home-made chemically-etched tungsten tips, annealed in UHV to bright orange color before being used for imaging.

ARPES measurements were carried out at the Advanced Light Source (ALS) endstation 7.0.2.1, and Stanford Synchrotron Research Laboratory (SSRL) beamlines 5-2 and 5-4. Data was taken with photon energies of 26 eV with linear horizontal polarization. Samples were cleaved *in situ* and measured under ultrahigh vacuum below 3×10^{-11} Torr at SSRL 5-4, 4×10^{-11} Torr at SSRL 5-2, and 2×10^{-11} Torr at ALS. Data was collected with Scienta R4000, DA30 L, and R4000 analyzers at SSRL 5-4, SSRL 5-2 and ALS, respectively.

III. RESULTS AND DISCUSSIONS

A. Growth optimization

Our initial trials of the CVT-growth of MnBi₂Te₂ were made in a Thermo Scientific muffle furnace rather than tube furnaces due to the two following considerations. First, the temperature profile of the CVT-growth is more delicate than the flux-growth of MnBi₂Te₄. The growth-end of the CVT-MnBi₂Te₄ should be kept at the temperature which is tested optimal for its flux growth. Second, a small temperature gradient of ~ 2 -3 K is sufficient and

essential for the success of the CVT growth. As shown in Figs. 1(b) and (c), when the CVT-growths are positioned in the furnace, the thermal gradient intrinsic to the box furnace, either vertically between the top and bottom of the furnace, or horizontally between the heating element to the furnace center, is responsible and sufficient for driving the vapor transport. The temperature gradient is indicated by the arrows in both Figs. 1(b) and (c), which is only 2-3 degrees from source to end.

Elemental form of Mn, Bi, Te and I are mixed according to the ratio of 1.7 : 2 : 4 : 1. Adding extra Mn or MnTe in the source end raises the melting point of the starting chunk, so it can remain as solid and allows a better control of its position at the source end during the transport. The elements were then sealed in a two-segment quartz tube as depicted in Fig. 1(b) or (c) under vacuum. The purpose of the two-segmented tube in a box furnace is to separate materials in the source (hot) and sink (cold) ends, and to have a balance over the cold-end area and transport rate so as to get sizable and abundant crystals. The quartz tube was then slowly heated to 900°C overnight to avoid over-pressure. Afterwards, the tube is air-quenched and transferred back to this box furnace preset at 585°C, which was pre-determined as the optimal temperature for our flux growth trials. In our trial-and-error process we find if the preset furnace temperature is too high, MnBi₂Te₄ in the cold end will be in the liquid form as condensed droplets; if the temperature is too low, mixed phases of Bi₂Te₃ and MnBi_{2n}Te_{3n+1} ($n \geq 2$) will form. It is noted that all I₂ is reacted in the first step of slow warming so MnI₂ becomes the effective transport agent. Within one week, mm-sized single crystals are obtained at the cold end of the growth together with red MnI₂. When samples are taken out, the mixtures from the cold end are rinsed with water to remove MnI₂ and to isolate the MnBi₂Te₄ crystals. A crystal grown with setup Fig. 1(b) is shown in the inset of Fig. 1(e).

With the experience of growing MnBi₂Te₄ in the box furnace, we can also accommodate the growth in a three-zone tube furnace. Here, a very careful calibration is needed ahead of the time at the exact location of both ends of the growth ampule. The furnace is set so that the cold end has the same temperature as that in the mid-bottom of the box furnace in Figs. 1(b)(c) and the hot end is merely 3 K hotter. The cold end is then nested within an additional alumina crucible so that the temperature gradient can be further smoothed near the end as shown in Fig. 1(d). Eventually MnBi₂Te₄ and MnI₂ crystals form and almost cover the cold end of the tube. Figure 1(d) includes a picture showing a plate “webbed” by MnBi₂Te₄ single crystals which were taken from a one-month growth in a 19-mm-diameter quartz tube and rinsed with water. With the careful calibration, the CVT-growth in the tube furnace can result in higher yields than both setups in box furnaces. The crystals in the “web” can be easily separated from each other for further measurements.

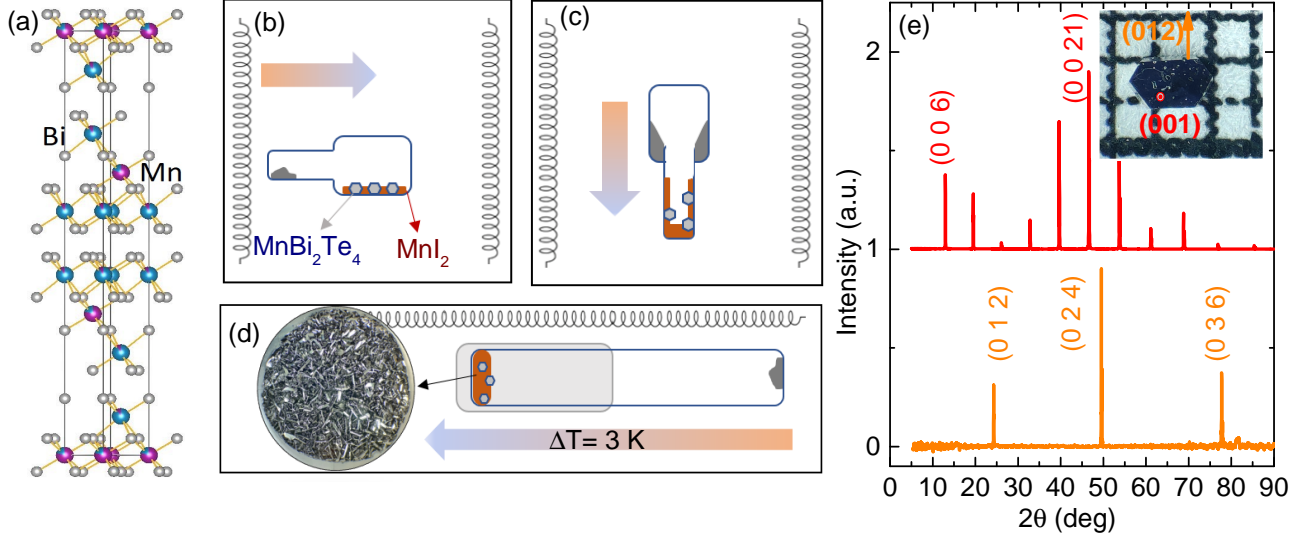


Figure 1. (a) Crystal structure of MnBi_2Te_4 with marked crystallographic Bi and Mn sites. Blue ball: Bi. Purple ball: Mn. Grey ball: Te. Mn site has Bi substitutions while the formation of Mn_{Bi} antisites results in a small amount of Mn atoms occupying the Bi site. (b)-(c) Schematics for the CVT growth, using the internal horizontal and vertical temperature gradient in a box furnace, respectively. The arrow indicates the gradient direction. (d) Schematics of the growth in a fine-tuned three zone furnace. Inset: mm-sized crystals after being taken out of a 19 mm-diameter tube and rinsed. (e) X-ray diffraction spectrum on the (001) surface and the (012) surface of a CVT-grown single crystal. Inset: a mm-sized hexagonal shaped single crystal from an one-week growth with marked surface indices.

Compared to the single crystal grown from other methods, the CVT samples tend to have a hexagonal shape with well-defined edges along the a and b directions. They can be up to 1 mm thick and appear more three-dimensional with flat and shiny edge surfaces. Hence in addition to the (00 L) reflections, other reflections such as (012) can be observed on the as-grown surfaces on the side, as shown in Fig. 1(e). The two surfaces giving the XRD pattern are indexed for the crystal in the inset of Fig. 1(e). The WDS conducted over 15 pieces of hexagonal crystals from several CVT batches finds an elemental ratio of $\text{Mn}_{0.94(3)}\text{Bi}_{2.09(7)}\text{Te}_4$ with no significant batch-to-batch variation. There is piece-to-piece variation. We note that pieces with six well-defined edges as shown in the inset of Fig. 1(e) in general have higher Mn concentrations than those with one as-grown edge. The highest Mn ratio is up to 0.98. In comparison, the elemental analysis on our flux-grown crystals finds $\text{Mn}_{0.90(1)}\text{Bi}_{2.08(5)}\text{Te}_4$. This suggests an overall enhancement of Mn concentration, and motivates us to look into its impact on the physical properties.

B. Physical properties

The effect of a higher Mn level in CVT samples can be reflected in the bulk magnetic and transport measurements. The results in Fig. 2 are measured on and compared between a CVT-grown sample (CVT-S1) with $\text{Mn}_{0.95}\text{Bi}_{2.09}\text{Te}_4$ and a flux-grown sample (flux-S1) with $\text{Mn}_{0.90}\text{Bi}_{2.11}\text{Te}_4$, each characterized with WDS. Figures.

2 (a) and (b) show the temperature-dependent susceptibility $\chi_{H\parallel c}$ and resistivity ρ_{xx} ($I//ab$). The AFM transition appears as a sharp kink in $\chi_{H\parallel c}(T)$ in both panels, which is found to be 24.6 K for CVT-S1 and 23.8 K for flux-S1. The drop of ρ_{xx} under T_N is consistent with the reduced spin-disorder scattering due to the formation of the in-plane ferromagnetic (FM) order.

The magnetism of MnBi_2Te_4 couples strongly with the charge carriers. The comparison of the magnetoresistance (MR), Hall resistivity, and magnetization under field between the two samples is included in Figs. 2 (c)-(e). From the slope of Hall resistivity near zero field or above 8 T, we calculate the electron-type carrier density at 2 K to be $5.1 \times 10^{19} \text{ cm}^{-3}$ and $1.5 \times 10^{20} \text{ cm}^{-3}$ for the CVT-S1 and flux-S1 sample, respectively. In Fig. 2(e), the magnetization per Mn is calculated based on the Mn concentration obtained from WDS. At 3.3 T for flux-S1, a feature from the spin-flop transition shows up across all three panels. The MR drops sharply with the sharp increase of the magnetic magnetization. In comparison, the CVT-S1 sample shows the same feature at 3.5 T. Then at 7.7 T, a feature due to the magnetic saturation is seen as a peak in MR and a subtle kink in Hall resistivity for both samples in Figs. 2 (c) and (d).

The magnetization data provides valuable insights on the distribution of Mn occupancy from the saturation moment. Since the $M(H)$ curve is linear between the flip-flop field and the saturation field, we can estimate the moment at the saturation field of 7.7 T for the two samples. The values are found to be $3.86 \mu_B/\text{Mn}$ for CVT-S1 and $3.94 \mu_B/\text{Mn}$ for flux-S1. Previous studies of

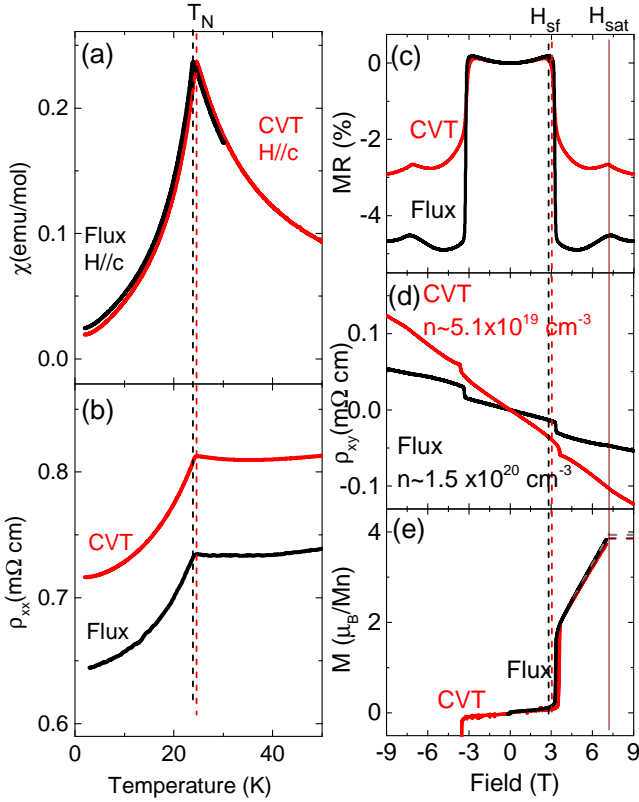


Figure 2. Comparison of the CVT-S1 and flux-S1 samples. (a)(b) Temperature-dependent magnetic susceptibility measured along H//c and longitudinal resistivity ρ_{xx} measured in the ab plane. (c)-(e) Field-dependent MR, Hall resistivity ρ_{xy} and the magnetization with marked spin-flop transition field and saturation field.

the sample grown by the flux method in Ref.⁴⁴ show that below 20 T, Mn on the Bi sites, which we call Mn2, aligns antiferromagnetically with the dominant Mn sublattice, which we call Mn1, creating a ferrimagnetic structure within each MnBi_2Te_4 SL. Therefore, the higher Mn2-to-Mn1 ratio, the smaller the “saturation” moment will be near 8 T. In our case, one can estimate the occupancy of Mn1 and Mn2 using

$$m_1 + 2m_2 = \text{Mn}_{\text{WDS}} \quad (1)$$

$$\frac{m_1 - 2m_2}{m_1 + 2m_2} = \frac{M_{8\text{T}}}{M_{50\text{T}}} \quad (2)$$

Here m_1 and m_2 are the occupancies of Mn1 and Mn2, respectively. Mn_{WDS} is the Mn concentration obtained from WDS. $M_{8\text{T}}$ is the initial saturation value estimated from the $M-H$ curve at 8 T where Mn1 and Mn2 are still AFM coupled. $M_{50\text{T}}$ is the final saturation value when Mn2 are also polarized to align in parallel with Mn1 at a high enough field, which is suggested to be $4.6\mu_B/\text{Mn}$ ⁴⁴. The values for m_1 and m_2 are 83.5% and 3.2% for flux-S1,

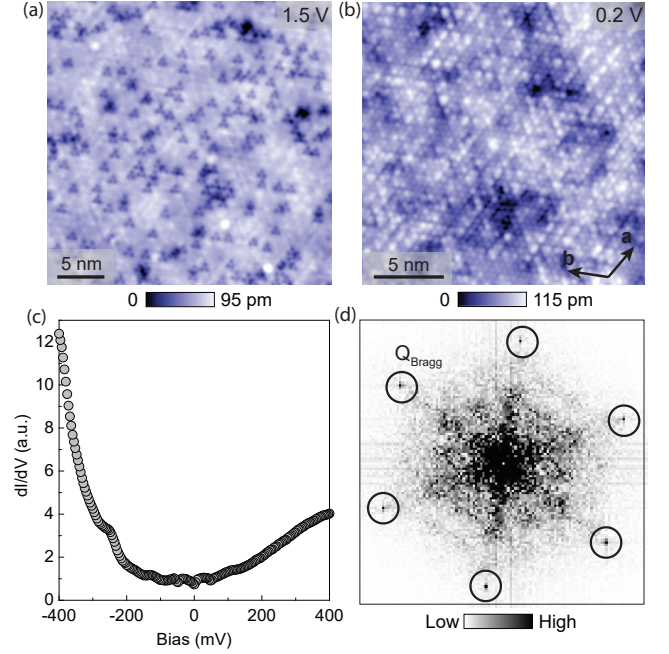


Figure 3. Scanning tunneling microscopy and spectroscopy of CVT-grown MnBi_2Te_4 . (a) Large-scale STM topograph showing a large, flat surface obtained by the cleaving process. Dark triangular features in the topograph represent Mn substitutions at the Bi site⁴³. (b) Zoom-in on a smaller region showing the expected hexagonal atomic structure. (c) Average dI/dV spectrum. (d) Fourier transform of the topograph in (b), with the atomic Bragg peaks denoted by black circles. STM setup condition: (a) 1.5 V/1.5 nA ; (b) 200 mV/200 pA; (c) 400 mV/300 pA (4 mV bias excitation). All data is acquired at 4.5 K.

and 87.4% and 3.8% for CVT-S1. The Mn concentrations are found to be higher in both sites in the CVT-S1, which reasonably explains why the magnetic transition temperature of CVT-S1 is higher. The higher Mn occupancy can also be associated with the reduced carrier concentration in the CVT-S1, since Bi atoms on Mn site is an electron-donor and makes the sample more n -type, while Mn on Bi site is an electron-acceptor⁴⁵ and makes the sample more p -type. Compared to the flux-S1 sample, the Mn1 occupancy of the CVT-S1 sample increases by 3.9% while the Mn2 occupancy only increases by 0.6%. This decreases the number of electron-donors and increases the number of electron-acceptors, thus making the sample less n -doped.

To observe the distribution of the defects and their effects on the electronic structure, STM was performed on a CVT-grown MnBi_2Te_4 . The CVT-grown single crystals were cleaved at room temperature at the pressure of 1×10^{-10} Torr and were immediately inserted into the STM head. Typical STM topographs show a flat surface with a hexagonal atomic structure (Fig. 3(a,b,d)), consistent with the expected MnBi_2Te_4 topmost surface layer composed of Te atoms. Dark triangular features in the

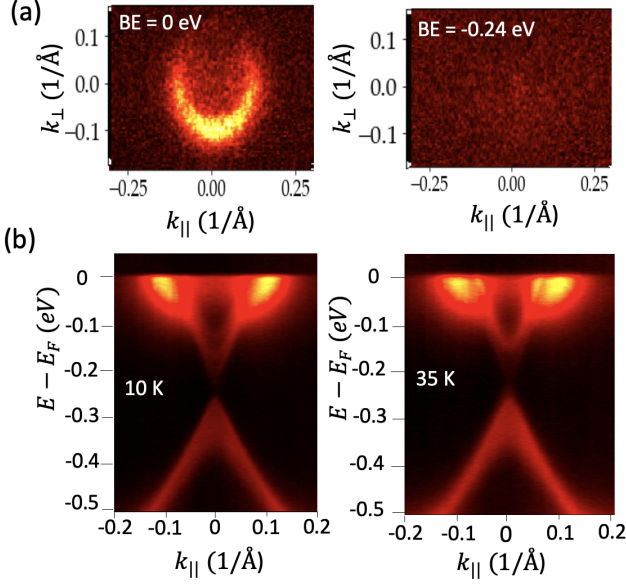


Figure 4. ARPES band maps and spectra on MnBi_2Te_4 sample CVT-S2. (a) ARPES intensity maps taken at E_F and the Dirac point at -0.24 eV binding energy. (b) ARPES spectra taken at 10 K and 35 K on the Γ to K cut, showing the TSS as well as a splitting of the bulk conduction band. ARPES data was taken with 26 eV, and the energy of the Dirac point is -0.24 eV, determined by finding the minimum of the energy distribution curve at Γ .

high-bias STM topograph in Fig. 3(a) can be identified as Mn substitutions at the Bi site⁴³. By manual counting of individual defects observed in the topograph, we calculate the density of these substitutions in our CVT samples to be around 3.5%. The antisite concentration is up from 3% in the STM of the flux-grown sample¹², suggesting a similar trend we found from our magnetization data. Lattice constant extracted from the Fourier transform (FT) of the topograph (Fig. 3(d)) is about 4.49 Å. Average dI/dV spectra show a sharp upturn in conductance at around -200 mV in Fig. 3(c). We note that this spectral feature is about 300 meV closer to the Fermi level compared to the spectra obtained in previous work^{12,38}, which may indicate a lower level of self-doping in our samples.

The effect of defects and charge carriers on the band structure can be seen more clearly with ARPES. The measurements were made on three different CVT-samples. CVT-S2 has 6 as-grown edges while CVT-S3 and CVT-S4 have only one as-grown edge. The topological surface state (TSS), along with bulk conduction and valence bands were observed. Figure 4 summarizes the ARPES data taken on CVT-S2. Figure 4(a) shows ARPES intensity maps at the Fermi energy, and at the Dirac point (DP) at -0.24 eV binding energy, respectively. Figure 4(b) shows the band structure of CVT-S2 cutting from the Γ point to K point in the Brillouin zone above and below the Néel temperature of 25 K. A

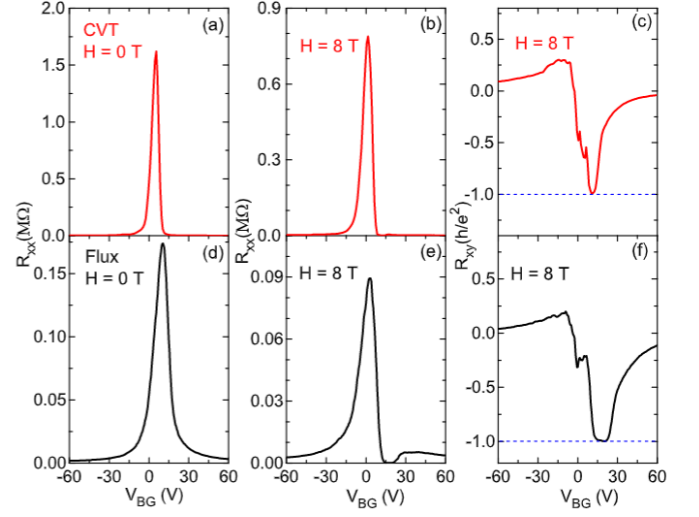


Figure 5. Observation of Chern insulator state in CVT and flux grown MnBi_2Te_4 . For the CVT-device and flux-grown MnBi_2Te_4 respectively: (a)(d) gate-voltage-dependent longitudinal resistance R_{xx} in the AFM state at zero field. At the gated charge neutrality point, $R_{xx}(T)$ in (a) is 10 times of that in (d) with a much sharper response to the gating voltage, suggesting better quality of the device. (b)(e) gate-voltage-dependent longitudinal resistance R_{xx} in the FM state at 8 T, with marked reduction of resistance near the charge neutrality point. (c)(f) gate-voltage-dependent Hall resistance R_{xy} in the FM state at 8 T, with marked quantized value of $\frac{h}{e^2}$ near the charge neutrality point.

splitting of the bulk conduction band is clearly observed below the Néel temperature in the 26-eV spectra, similar to previous reports on samples grown by the flux method or stoichiometric melting^{18,46}. The energies of the Dirac point can be estimated as the minimum of the energy distribution curve at the Γ point. It is -0.24 eV for CVT-S2, -0.26 eV for CVT-S3, and -0.275 eV for CVT-S4. This variation in energy is consistent with what we have learned from our WDS measurements, that is, the well-shaped CVT crystals have higher Mn concentrations. In previous measurements on flux-grown samples, the DP energy ranges from -0.275 eV to -0.28 eV binding energy^{17,19,47}, and samples grown with stoichiometric melting have DP energies at -0.27 and -0.275 eV binding energy^{18,46}. Therefore, compared to flux-grown samples, the CVT-grown samples are in general more intrinsic. Especially, for the hexagonal-shaped CVT-2, the DP is around 35 meV lower and closer to the TSS. This is again consistent with the lower carrier concentration extracted from the Hall resistivity.

C. Chern insulator state in 2D limit

To investigate the transport properties of the CVT-grown samples in the 2D limit, we exfoliated the MnBi_2Te_4 samples down to the atomically thin regime

and fabricated 2D quantum devices. Figures 5 (a)-(c) show representative data of a 6-SL device made of a CVT grown MnBi_2Te_4 crystal. In the AFM phase ($H = 0$), our transport measurement (Fig. 5 (a)) shows a clear insulating behavior with the resistance reaching over 10^6 Ohms. This agrees with the theoretical expectation that the 6-SL AFM MnBi_2Te_4 is an Axion insulator with zero Chern number. Notably, as shown in Fig. 5 (a), the gate voltage that corresponds to the charge neutrality in the CVT-device is very close to $V_{BG}=0$ V. This indicates that natural doping in this 6-SL MnBi_2Te_4 device is small, consistent with the reduced carrier density that we obtained from the bulk transport measurements. Based on the field effect model, we estimate a carrier mobility of ~ 2500 $\text{cm}^2/\text{V}\cdot\text{s}$, which is the highest that has ever been reported. In the FM phase ($H=8$ T), our transport data reveal a fully vanishing longitudinal resistance R_{xx} and fully quantized Hall resistance, which demonstrate the topological Chern insulator state, consistent with previous studies^{15,16}.

We further compare this 6-SL device using the CVT-grown MnBi_2Te_4 crystal with a 6-SL device using a flux-grown MnBi_2Te_4 crystal. As shown in Fig. 5, the two devices show qualitatively similar behaviors, i.e., an insulating behavior in the AFM phase and a topological Chern insulator behavior with quantized Hall response in the FM phase. We note that the Chern insulator behavior appears in a narrower range of gate voltage in the CVT-device. This may be related to the larger amount of antisite disorder present in the CVT-crystal. Despite this, the CVT-devices have a higher success rate in realizing the Chern insulator state, which is likely to be attributed to the high Mn1 concentration that gives higher magnetic homogeneity. Meanwhile, by comparing Figs. 5 (a)(b) and (d)(e), one can clearly see that the resistance peak is much sharper and higher for the CVT-device as a result of the larger carrier mobility. Based on the field effect model, carrier mobility of the flux-device is found ~ 800 $\text{cm}^2/\text{V}\cdot\text{s}$, which is around one third of the CVT one.

IV. CONCLUSION

In summary, compared with the flux-grown MnBi_2Te_4 single crystals, the CVT-grown ones have less Bi sub-

stitution on the Mn site and slightly more Mn_{Bi} antisites, leading to a smaller carrier density and reduced energy difference between the Fermi level and the Dirac point in bulk CVT-sample. Furthermore, when exfoliated into 6-SL device, the CVT samples show by far the highest mobility of 2500 $\text{cm}^2/\text{V}\cdot\text{s}$ with vanishing R_{xx} and quantized R_{xy} at 8 T. Therefore, our new growth design readily allowed us to achieve devices with higher quality. This paves a new way to optimize crystal growth of MnBi_2Te_4 and related $\text{MnBi}_{2n}\text{Te}_{3n+1}$ ($n \geq 2$) to investigate the emergent phenomena arising from the interplay of topology and the magnetism. Future optimization such as varying the Mn concentration in the source end, using other transport agents such as TeI_4 , etc. can be explored to further improve the sample quality.

ACKNOWLEDGMENTS

We thank Peipei Hao, Garrison Linn, Makoto Hashimoto, Donghui Lu, Chris Jozwiak, and Jonathan Denlinger for the help on ARPES measurements and useful discussions. Work at UCLA was supported by the U.S. Department of Energy (DOE), Office of Science, Office of Basic Energy Sciences under Award Number DE-SC0021117. Work at Harvard was supported by the Center for the Advancement of Topological Semimetals, an Energy Frontier Research Center funded by the U.S. Department of Energy (DOE) Office of Science, through the Ames Laboratory under contract DE-AC0207CH11358 (device fabrication) and by the STC Center for Integrated Quantum Materials (CIQM), NSF Grant No. DMR-1231319 (measurements). Work at CU-Boulder was funded by the U.S. DOE, Office of Science, Office of Basic Energy Sciences under Award Number DE-FG02-03ER46066. The ARPES work used resources of the Advanced Light Source, a U.S. DOE Office of Science User Facility under contract no. DE-AC02-05CH11231. Use of the Stanford Synchrotron Radiation Lightsource, SLAC National Accelerator Laboratory, is supported by the US DOE, Office of Science, Office of Basic Energy Sciences under Contract No. DE-AC02-76SF00515. Work at Boston College was supported by the National Science Foundation grant no. NSF-DMR-1654041 for the STM work. CH thanks the support by the Julian Schwinger Fellowship at UCLA.

* Corresponding author: nini@physics.ucla.edu

¹ K. He, Y. Wang, and Q.-K. Xue, Annual Review of Condensed Matter Physics **9**, 329 (2018).

² C.-X. Liu, S.-C. Zhang, and X.-L. Qi, Annual Review of Condensed Matter Physics **7**, 301 (2016).

³ J. Wang, B. Lian, X.-L. Qi, and S.-C. Zhang, Physical Review B **92**, 081107 (2015).

⁴ D. S. Lee, T.-H. Kim, C.-H. Park, C.-Y. Chung, Y. S. Lim, W.-S. Seo, and H.-H. Park, CrystEngComm **15**, 5532 (2013).

⁵ E. Rienks, S. Wimmer, J. Sánchez Barriga, O. Caha, P. Mandal, J. Růžička, A. Ney, H. Steiner, V. Volobuev, H. Groiss, *et al.*, Nature **576**, 423 (2019).

⁶ D. Zhang, M. Shi, T. Zhu, D. Xing, H. Zhang, and J. Wang, Physical review letters **122**, 206401 (2019).

- ⁷ J. Li, Y. Li, S. Du, Z. Wang, B.-L. Gu, S.-C. Zhang, K. He, W. Duan, and Y. Xu, *Science Advances* **5**, eaaw5685 (2019).
- ⁸ M. M. Otrokov, I. I. Klimovskikh, H. Bentmann, D. Estyunin, A. Zeugner, Z. S. Aliev, S. Gaß, A. Wolter, A. Koroleva, A. M. Shikin, *et al.*, *Nature* **576**, 416 (2019).
- ⁹ Z. S. Aliev, I. R. Amiraslanov, D. I. Nasonova, A. V. Shevelkov, N. A. Abdullayev, Z. A. Jahangirli, E. N. Orujlu, M. M. Otrokov, N. T. Mamedov, M. B. Babanly, *et al.*, *Journal of Alloys and Compounds* **789**, 443 (2019).
- ¹⁰ Y. Gong, J. Guo, J. Li, K. Zhu, M. Liao, X. Liu, Q. Zhang, L. Gu, L. Tang, X. Feng, *et al.*, *Chinese Physics Letters* **36**, 076801 (2019).
- ¹¹ S. H. Lee, Y. Zhu, Y. Wang, L. Miao, T. Pillsbury, H. Yi, S. Kempinger, J. Hu, C. A. Heikes, P. Quarterman, *et al.*, *Physical Review Research* **1**, 012011 (2019).
- ¹² J.-Q. Yan, Q. Zhang, T. Heitmann, Z. Huang, K. Chen, J.-G. Cheng, W. Wu, D. Vaknin, B. C. Sales, and R. J. McQueeney, *Physical Review Materials* **3**, 064202 (2019).
- ¹³ A. Zeugner, F. Nietschke, A. U. Wolter, S. Gaß, R. C. Vidal, T. R. Peixoto, D. Pohl, C. Damm, A. Lubk, R. Henrich, *et al.*, *Chemistry of Materials* **31**, 2795 (2019).
- ¹⁴ M. M. Otrokov, I. P. Rusinov, M. Blanco-Rey, M. Hoffmann, A. Y. Vyazovskaya, S. V. Eremeev, A. Ernst, P. M. Echenique, A. Arnau, and E. V. Chulkov, *Physical Review Letters* **122**, 107202 (2019).
- ¹⁵ Y. Deng, Y. Yu, M. Z. Shi, Z. Guo, Z. Xu, J. Wang, X. H. Chen, and Y. Zhang, *Science* **367**, 895 (2020).
- ¹⁶ C. Liu, Y. Wang, H. Li, Y. Wu, Y. Li, J. Li, K. He, Y. Xu, J. Zhang, and Y. Wang, *Nature Materials* **19**, 522 (2020).
- ¹⁷ Y.-J. Hao, P. Liu, Y. Feng, X.-M. Ma, E. F. Schwier, M. Arita, S. Kumar, C. Hu, M. Zeng, Y. Wang, *et al.*, *Physical Review X* **9**, 041038 (2019).
- ¹⁸ Y. Chen, L. Xu, J. Li, Y. Li, H. Wang, C. Zhang, H. Li, Y. Wu, A. Liang, C. Chen, *et al.*, *Physical Review X* **9**, 041040 (2019).
- ¹⁹ H. Li, S.-Y. Gao, S.-F. Duan, Y.-F. Xu, K.-J. Zhu, S.-J. Tian, J.-C. Gao, W.-H. Fan, Z.-C. Rao, J.-R. Huang, *et al.*, *Physical Review X* **9**, 041039 (2019).
- ²⁰ B. Li, J.-Q. Yan, D. M. Pajerowski, E. Gordon, A.-M. Nedić, Y. Sizyuk, L. Ke, P. P. Orth, D. Vaknin, and R. J. McQueeney, *Physical review letters* **124**, 167204 (2020).
- ²¹ L. Ding, C. Hu, F. Ye, E. Feng, N. Ni, and H. Cao, *Physical Review B* **101**, 020412 (2020).
- ²² C. Hu, K. N. Gordon, P. Liu, J. Liu, X. Zhou, P. Hao, D. Narayan, E. Emmanouilidou, H. Sun, Y. Liu, *et al.*, *Nature communications* **11**, 1 (2020).
- ²³ S. Tian, S. Gao, S. Nie, Y. Qian, C. Gong, Y. Fu, H. Li, W. Fan, P. Zhang, T. Kondo, S. Shin, J. Adell, H. Fedderwitz, H. Ding, Z. Wang, T. Qian, and H. Lei, *Phys. Rev. B* **102**, 035144 (2020).
- ²⁴ C. Hu, L. Ding, K. N. Gordon, B. Ghosh, H.-J. Tien, H. Li, A. G. Linn, S.-W. Lien, C.-Y. Huang, S. Mackey, *et al.*, *Science Advances* **6**, eaba4275 (2020).
- ²⁵ H. Deng, Z. Chen, A. Wołoś, M. Konczykowski, K. Sobczak, J. Sitnicka, I. V. Fedorchenko, J. Borysiuk, T. Heider, L. Pluciński, *et al.*, *Nature Physics* **17**, 36 (2021).
- ²⁶ M. Shi, B. Lei, C. Zhu, D. Ma, J. Cui, Z. Sun, J. Ying, and X. Chen, *Physical Review B* **100**, 155144 (2019).
- ²⁷ J. Wu, F. Liu, M. Sasase, K. Ienaga, Y. Obata, R. Yukawa, K. Horiba, H. Kumigashira, S. Okuma, T. Inoshita, *et al.*, *Science advances* **5**, eaax9989 (2019).
- ²⁸ J.-Q. Yan, Y. Liu, D. Parker, Y. Wu, A. Aczel, M. Matsuda, M. McGuire, and B. Sales, *Physical Review Materials* **4**, 054202 (2020).
- ²⁹ K. N. Gordon, H. Sun, C. Hu, A. G. Linn, H. Li, Y. Liu, P. Liu, S. Mackey, Q. Liu, N. Ni, *et al.*, arXiv preprint arXiv:1910.13943 (2019).
- ³⁰ Y. Hu, L. Xu, M. Shi, A. Luo, S. Peng, Z. Wang, J. Ying, T. Wu, Z. Liu, C. Zhang, *et al.*, *Physical Review B* **101**, 161113 (2020).
- ³¹ L. Xu, Y. Mao, H. Wang, J. Li, Y. Chen, Y. Xia, Y. Li, J. Zhang, H. Zheng, K. Huang, *et al.*, arXiv preprint arXiv:1910.11014 (2019).
- ³² N. H. Jo, L.-L. Wang, R.-J. Slager, J. Yan, Y. Wu, K. Lee, B. Schunk, A. Vishwanath, and A. Kaminski, *Physical Review B* **102**, 045130 (2020).
- ³³ A. Tan, V. Labracherie, N. Kunchur, A. U. Wolter, J. Cornejo, J. Dufouleur, B. Büchner, A. Isaeva, and R. Giraud, *Physical Review Letters* **124**, 197201 (2020).
- ³⁴ I. I. Klimovskikh, M. M. Otrokov, D. Estyunin, S. V. Eremeev, S. O. Filnov, A. Koroleva, E. Shevchenko, V. Voroshnin, A. G. Rybkin, I. P. Rusinov, *et al.*, npj Quantum Materials **5**, 1 (2020).
- ³⁵ Z. Zhao, C. Hu, A. Kavner, N. Ni, and C. W. Wong, in *2020 Conference on Lasers and Electro-Optics (CLEO) (IEEE, 2020)* pp. 1–2.
- ³⁶ R. Vidal, H. Bentmann, J. Facio, P. Kagerer, C. Fornari, T. Peixoto, T. Figgemeier, S. Jung, C. Cacho, B. Büchner, *et al.*, arXiv preprint arXiv:2007.07637 (2020).
- ³⁷ Z. Huang, M.-H. Du, J. Yan, and W. Wu, *Physical Review Materials* **4**, 121202 (2020).
- ³⁸ Y. Yuan, X. Wang, H. Li, J. Li, Y. Ji, Z. Hao, Y. Wu, K. He, Y. Wang, Y. Xu, *et al.*, *Nano letters* **20**, 3271 (2020).
- ³⁹ J.-Q. Yan, S. Okamoto, M. A. McGuire, A. F. May, R. J. McQueeney, and B. C. Sales, *Physical Review B* **100**, 104409 (2019).
- ⁴⁰ A. Gao, Y.-F. Liu, C. Hu, J.-X. Qiu, C. Tzschaschel, B. Ghosh, S.-C. Ho, D. Bérubé, R. Chen, H. Sun, *et al.*, *Nature* **595**, 521 (2021).
- ⁴¹ Y. Liu, L.-L. Wang, Q. Zheng, Z. Huang, X. Wang, M. Chi, Y. Wu, B. C. Chakoumakos, M. A. McGuire, B. C. Sales, *et al.*, *Physical Review X* **11**, 021033 (2021).
- ⁴² C. Hu, S.-W. Lien, E. Feng, S. Mackey, H.-J. Tien, I. I. Mazin, H. Cao, T.-R. Chang, and N. Ni, *Phys. Rev. B* **104**, 054422 (2021).
- ⁴³ Y. Hor, P. Roushan, H. Beidenkopf, J. Seo, D. Qu, J. Checkelsky, L. Wray, D. Hsieh, Y. Xia, S.-Y. Xu, *et al.*, *Physical Review B* **81**, 195203 (2010).
- ⁴⁴ Y. Lai, L. Ke, J. Yan, R. D. McDonald, and R. J. McQueeney, *Physical Review B* **103**, 184429 (2021).
- ⁴⁵ M.-H. Du, J. Yan, V. R. Cooper, and M. Eisenbach, *Advanced Functional Materials* **31**, 1 (2021).
- ⁴⁶ D. A. Estyunin, I. I. Klimovskikh, A. M. Shikin, E. F. Schwier, M. M. Otrokov, A. Kimura, S. Kumar, S. O. Filnov, Z. S. Aliev, M. B. Babanly, and E. V. Chulkov, *APL Materials* **8**, 021105 (2020).
- ⁴⁷ P. Swatek, Y. Wu, L.-L. Wan, K. Lee, B. Schunk, J. Yan, and A. Kaminski, *Physical Review B* **101**, 161109(R) (2020).